

## pH Effects in a Model Electrocatalytic Reaction Disentangled

Xinwei Zhu, Jun Huang, and Michael Eikerling\*



Cite This: JACS Au 2023, 3, 1052–1064



Read Online

ACCESS |



Metrics &amp; More



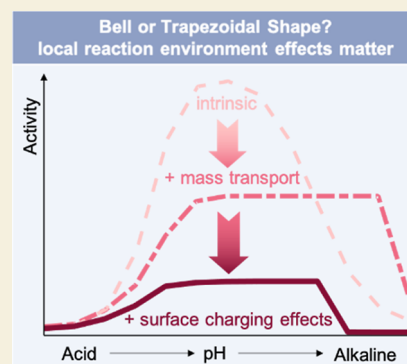
Article Recommendations



Supporting Information

**ABSTRACT:** Varying the solution pH not only changes the reactant concentrations in bulk solution but also the local reaction environment (LRE) that is shaped furthermore by macroscopic mass transport and microscopic electric double layer (EDL) effects. Understanding ubiquitous pH effects in electrocatalysis requires disentangling these interwoven factors, which is a difficult, if not impossible, task without physical modeling. Herein, we demonstrate how a hierarchical model that integrates microkinetics, double-layer charging, and macroscopic mass transport can help understand pH effects of the formic acid oxidation reaction (FAOR). In terms of the relation between the peak activity and the solution pH, intrinsic pH effects without consideration of changes in the LRE would lead to a bell-shaped curve with a peak at pH = 6. Adding only macroscopic mass transport, we can already reproduce qualitatively the experimentally observed trapezoidal shape with a plateau between pH 5 and 10 in perchlorate and sulfate solutions. A quantitative agreement with experimental data requires consideration of EDL effects beyond Frumkin correlations. Specifically, the peculiar nonmonotonic surface charging relation affects the free energies of adsorbed intermediates. We further discuss pH effects of FAOR in phosphate and chloride-containing solutions, for which anion adsorption becomes important. This study underpins the importance of a full consideration of multiple interrelated factors for the interpretation of pH effects in electrocatalysis.

**KEYWORDS:** pH effects, local reaction environment, electric double layer, mass transport, surface charging effects, formic acid oxidation reaction



## INTRODUCTION

Electrocatalysis, which refers to heterogeneous catalysis of electrochemical reactions that occur at the electrode–electrolyte interface, is the key discipline to enable a sustainable and environmentally benign global energy infrastructure. A quintessential aspect of electrocatalysis is that the activity of a particular reaction can vary over several orders of magnitude if different electrode materials or atomic surface configurations are used.<sup>1–3</sup> In the past decades, remarkable progress in understanding the role of the electrode material has paved the way toward rational designs of electrocatalysts.<sup>1–8</sup> The role of other medium involved in electrocatalysis, viz. the electrolyte, is however much less understood. Controversy exists over how the type and concentration of cations modulate the reaction activity,<sup>9–12</sup> and why variations in solution pH cause activity differences of several orders of magnitude for specific reactions.<sup>13–18</sup>

Various explanations of pH effects in electrocatalytic reactions have been given, including shifts of bulk proton concentration and electrode potential on the standard hydrogen electrode (SHE) scale,<sup>18,19</sup> changes in proton donor or oxidant,<sup>14,20,21</sup> and modulations on possible solution-phase reactions.<sup>22–24</sup> In addition to these overall properties, local properties in the electric double layer (EDL), including local potential, concentration, and electric field, can also change with the solution pH. Recent years have witnessed

growing attention to these local reaction environment (LRE) effects. For instance, macroscopic mass transport induces departure of the local pH from the bulk pH during the formic acid oxidation reaction (FAOR).<sup>25,26</sup> Additionally, the local reactant concentration, which is lower than the bulk concentration due to the macroscopic mass transport, is a key factor to understand pH effects on the hydrogen evolution/oxidation reaction (HER/HOR)<sup>14,27</sup> and the CO<sub>2</sub> electrochemical reduction reaction (CO<sub>2</sub>ER).<sup>28,29</sup> It has also been demonstrated that the electric field in the EDL impacts free energies of intermediates in the oxygen reduction reaction<sup>30,31</sup> and the CO electrochemical reduction.<sup>9,32</sup> Lastly, the role of the reorganization of interfacial water affected by the electric field is highlighted in the HER.<sup>33,34</sup> These studies have shown that apparent pH effects are the consequence of multiple interacting factors. Any endeavor toward a comprehensive understanding should be aware of their interplay and find a proper way to disentangle them, which is highly nontrivial even for simple model reactions, such as HER and

Received: December 6, 2022

Revised: February 9, 2023

Accepted: February 15, 2023

Published: March 1, 2023



FAOR.<sup>34,35</sup> Theory and modeling are indispensable to this end.<sup>1,2,15</sup>

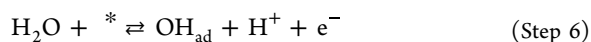
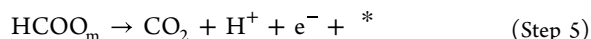
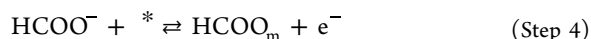
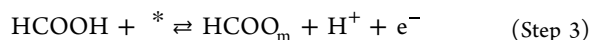
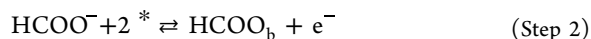
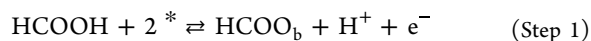
In this work, we aim to disentangle the aforementioned multiple factors that affect the FAOR at single crystals. Marked pH effects have been reported by several independent groups for this model system, but the explanations given have remained controversial. The controversy on reproducible experimental phenomena in the simplest model system just indicates the complexity arising from multiple interacting factors, as well as the lack of a reliable approach to handle the complexity. We carefully analyze experimental data using a set of models that gradually climb the ladder of complexity, in order to avoid overfitting of experimental data. Our incremental analysis underlines the importance of considering LRE in understanding experimental pH effects. Specifically, we find that a quantitative analysis of experiments requires taking into account EDL effects that go beyond Frumkin corrections but were not considered in previous studies.

## MODEL DEVELOPMENT

We model the oxidation of formic acid for a system consisting of a rotating Pt(111) disk electrode (RDE) in 0.5 M perchlorate solutions under ambient conditions (25 °C, 101.3 kPa). The pH range from 0 to 12 is considered. The model consists of a microkinetic submodel that determines the adsorbate coverages and current densities and a modified Poisson–Nernst–Planck (PNP) submodel that determines the LRE, namely, the distributions of potential and species concentrations at or near the reaction plane (RP).

### Microkinetics

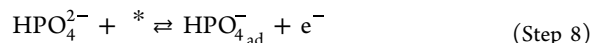
The reaction mechanism used in this model involves three adsorbates, HCOO<sub>b</sub>, HCOO<sub>m</sub>, and OH<sub>ad</sub>.<sup>36</sup>



Bridge-bonded formate HCOO<sub>b</sub> was detected on Pt electrodes by surface-enhanced IR absorption spectroscopy.<sup>37</sup> However, HCOO<sub>b</sub> is unlikely to be the main active intermediate because density functional theory (DFT) calculations have shown that its oxidation barrier is too high (~1.1 eV).<sup>38,39</sup> *In situ* IR studies have shown that HCOO<sub>b</sub> is a site-blocking spectator.<sup>40,41</sup> Therefore, the oxidation step of HCOO<sub>b</sub> should be negligible. It has then been speculated that there must be other active intermediates, which, due to their short lifetime and/or low coverage, were not detected in spectroscopic measurements.<sup>41</sup> DFT calculations have proposed two candidates, COOH<sub>ad</sub><sup>42</sup> and C–H down monodentate formate HCOO<sub>m</sub>.<sup>43,44</sup> Following studies on the pH effects of FAOR,<sup>24,45–47</sup> we consider HCOO<sub>m</sub> as the main active intermediate. Herein, we have negligible adsorbed CO<sub>ad</sub> because CO<sub>ad</sub> is considered to be absent on defect-free Pt(111).<sup>48</sup> In addition, cyclic voltammetry data in the negative

scan during which CO<sub>ad</sub> is oxidized are used for the analysis.<sup>45,49,50</sup> In addition to the main reactions, this model also considers water oxidation at high potentials that forms site-blocking OH<sub>ad</sub>.

For the case of phosphate solutions, the FAOR is inhibited when pH > 4.<sup>45,51</sup> This is the pH range in which HPO<sub>4</sub><sup>2−</sup> appears. Therefore, we consider the adsorption of HPO<sub>4</sub><sup>2−</sup>



For the case of chloride-containing solutions, anion adsorption is accounted for *via*



Based on the postulated reaction mechanism, rate equations for the changes of adsorbate coverages, which are zero at steady state, can be formulated

$$\frac{d\theta_{\text{HCOO}_b}}{dt} = \nu_1 + \nu_2 \quad (1)$$

$$\frac{d\theta_{\text{HCOO}_m}}{dt} = \nu_3 + \nu_4 - \nu_5 \quad (2)$$

$$\frac{d\theta_{\text{OH}_{ad}}}{dt} = \nu_6 + \nu_7 \quad (3)$$

$$\frac{d\theta_{\text{HPO}_4^-_{ad}}}{dt} = \nu_8 \quad (4)$$

$$\frac{d\theta_{\text{Cl}_{ad}}}{dt} = \nu_9 \quad (5)$$

where  $\theta_{\text{HCOO}_b}$ ,  $\theta_{\text{HCOO}_m}$ ,  $\theta_{\text{OH}_{ad}}$ ,  $\theta_{\text{HPO}_4^-_{ad}}$ , and  $\theta_{\text{Cl}_{ad}}$  are coverages and  $\nu_i$  is the reaction rate of step  $i$

$$\nu_i = k_{+i} \prod c_i \theta_i - k_{-i} \prod c_{-i} \theta_{-i} \quad (6)$$

where  $c_i$  and  $\theta_i$ ,  $c_{-i}$ , and  $\theta_{-i}$  are species concentrations and intermediate coverages involved in forward and backward reactions of step  $i$ . The rate constants  $k_{+i}$  and  $k_{-i}$  are obtained from transition-state theory

$$k_{\pm i} = \frac{k_B T}{h} \exp\left(-\frac{G_{a,\pm i}}{k_B T}\right) \quad (7)$$

with  $k_B$  being the Boltzmann constant,  $T$  the temperature, and  $h$  the Planck constant. Activation energies,  $G_{a,\pm i}$ , under standard conditions (298 K, 1 bar pressure, pH = 0) are determined using the Brønsted–Evans–Polanyi (BEP) relation<sup>52</sup>

$$G_{a,+i} = G_{a,i}^{\text{eq}} + \beta_i \Delta G_i \quad (8)$$

$$G_{a,-i} = G_{a,i}^{\text{eq}} - (1 - \beta_i) \Delta G_i \quad (9)$$

where  $G_{a,i}^{\text{eq}}$  is the activation energy of step  $i$  under standard equilibrium conditions,  $\beta_i$  is the transfer coefficient, and  $\Delta G_i$  is the reaction Gibbs free energy, which shifts with potential according to

$$\Delta G_i = -e(E_M - \varphi_{\text{RP}} - E_i^{\text{eq}}) + \Delta \Delta G_i \quad (10)$$

Here,  $e$  is the elementary charge,  $E_M$  is the applied potential relative to the SHE, and  $\varphi_{\text{RP}}$  is the potential at the RP, which needs to be determined with the PNP submodel.  $E_i^{\text{eq}}$  is the

equilibrium potential of step  $i$  and is calculated using the Nernst equation

$$E_i^{\text{eq}} = \Delta G_i^0 / e \quad (11)$$

with  $\Delta G_i^0$  being the reaction free energy of step  $i$  at the standard state, which can be determined with the aid of DFT.  $\Delta \Delta G_i$  represents the variations in the Gibbs free energy caused by lateral interactions between adsorbates and surface charging effects.

$\theta_{\text{HCOO}_b}$ ,  $\theta_{\text{HCOO}_m}$ ,  $\theta_{\text{OH}_{ad}}$ ,  $\theta_{\text{HPO}_4^-}$ , and  $\theta_{\text{Cl}_{ad}}$  are obtained by solving eqs 1–5. The partial current densities are given by

$$j_{\text{HCOOH}} = -2e\rho v_3 \quad (12)$$

$$j_{\text{HCOO}^-} = -2e\rho v_4 \quad (13)$$

$$j_{\text{H}^+} = -\left(j_{\text{HCOOH}} + \frac{j_{\text{HCOO}^-}}{2}\right) \quad (14)$$

$$j = 2e\rho v_5 \quad (15)$$

with  $\rho$  the number density of active sites at Pt(111) and  $e\rho = 2.41 \text{ C/m}^2$  in this model.<sup>53</sup> The details and parameters of the microkinetic model can be found in the [Supporting Information](#).

### Local Reaction Environment

The model system is shown in [Figure 1](#). We consider an adlayer between the electrode and the electrolyte, in which the

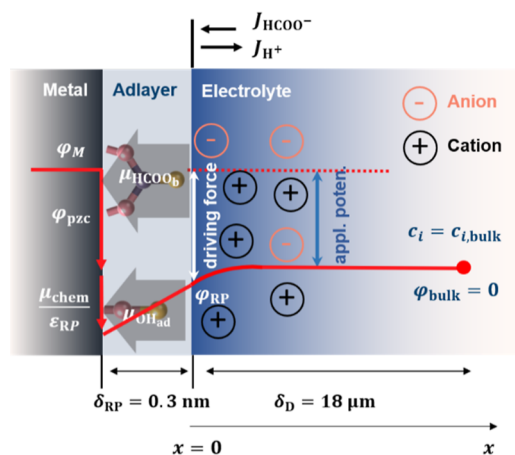


**Figure 1.** Schematic illustration of the model system. Two zones at the electrode–electrolyte surface are distinguished: the adlayer and the boundary layer in the electrolyte. The RP is located at the boundary between them, where the fluxes are indicated. The solid red line is a schematic potential profile for the case of negative surface charge, with  $\phi_M$  denoting the applied metal potential and  $\phi_{\text{pzc}}$  the potential of zero charge.  $\mu_{\text{chem}}$  is the dipole moment associated with chemisorbed  $\text{HCOO}_b$  and  $\text{OH}_{ad}$ . The driving force for interface reactions is defined as the difference between the applied potential  $\phi_M$  and the potential at the RP  $\phi_{\text{RP}}$ .  $\delta_{\text{RP}}$  and  $\delta_D$  are the thicknesses of adlayer and diffusion layer, respectively.

intermediates are adsorbed, and the potential distribution across the adlayer is considered to be linear. The RP is located at the outer surface of the adlayer ( $x = 0$ ), which is also the position of the closest ion. Outside the RP resides the diffusion layer, whose thickness is determined as<sup>54</sup>

$$\delta_D = 1.62 D_{\text{HCOO}^-}^{1/3} \nu^{1/6} \omega^{-1/2} \quad (16)$$

where  $D_{\text{HCOO}^-}$  is the diffusion coefficient of  $\text{HCOO}^-$ ,  $\nu$  is the kinematic viscosity of the solution phase, and  $\omega$  is the rotation speed of the RDE. We use  $D_{\text{HCOO}^-}$  to calculate the diffusion layer thickness since  $\text{HCOO}^-$  is the main reactant.

The modified Nernst–Planck equation, which takes into account steric effects,<sup>55,56</sup> is used to model mass transport of  $\text{HCOOH}$ ,  $\text{HCOO}^-$ ,  $\text{OH}^-$ ,  $\text{ClO}_4^-$ ,  $\text{H}^+$ ,  $\text{Na}^+$ ,  $\text{H}_3\text{PO}_4$ ,  $\text{H}_2\text{PO}_4^-$ ,  $\text{HPO}_4^{2-}$ , and  $\text{PO}_4^{3-}$

$$\frac{\partial c_i}{\partial t} = -\nabla \cdot J_i + R_i \quad (17)$$

$$J_i = -D_i \left( \left( 1 - \sum_{j \neq i} N_A a_j^3 c_j \right) \frac{\partial c_i}{\partial x} + c_i \sum_{j \neq i} N_A a_j^3 \frac{\partial c_j}{\partial x} + \frac{z_i F}{RT} c_i \left( 1 - \sum_j N_A a_j^3 c_j \right) \frac{\partial \phi}{\partial x} \right) \quad (18)$$

where  $c_i$  is the concentration,  $R_i$  is the source term due to homogeneous reactions (cf. [Supporting Information Note S2](#)),  $J_i$  is the flux,  $D_i$  is the diffusion coefficient,  $N_A$  is the Avogadro constant,  $a_i$  is the effective diameter,  $z_i$  is the charge number,  $F$  is the Faraday constant,  $R$  is the ideal gas constant, and  $\phi$  is the local electric potential.

The Nernst–Planck equation is complemented by the Poisson equation

$$-\nabla \cdot (\epsilon_s \nabla \phi) = F \sum_i z_i c_i \quad (19)$$

with  $\epsilon_s$  being the permittivity of the electrolyte.

To solve the PNP equations, boundary conditions are needed. At the right side of the domain shown in [Figure 1](#) ( $x = \delta_D$ ), concentrations are equal to bulk concentrations, i.e.,  $c_i = c_{i,\text{bulk}}$ . The potential at this position is taken as the reference potential,  $\phi_{\text{bulk}} = 0$ . The left side ( $x = 0$ ) corresponds to the RP. The fluxes at this position are given by

$$J_i = \frac{j_i}{n_{e,i} F} \quad (20)$$

where  $j_i$  is the partial current density that consumes ( $j_i < 0$ ) or generates ( $j_i > 0$ ) species  $i$ , as described in eqs 12–14, and  $n_{e,i}$  is the number of electrons involved in the reaction. We have  $n_{e,\text{HCOOH}} = n_{e,\text{HCOO}^-} = 2$ ,  $n_{e,\text{H}^+} = 1$ , and  $J_i = 0$  for other species. The boundary condition for the potential is given by a Robin-type boundary condition<sup>55,57</sup>

$$\sigma_M = -\epsilon_s \frac{\partial \phi}{\partial x} \Big|_{x=0} = \frac{\epsilon_{\text{RP}}}{\delta_{\text{RP}}} \left( \phi_M - \phi_{\text{pzc}} - \frac{\mu_{\text{chem}}}{\epsilon_{\text{RP}}} - \phi|_{x=0} \right) \quad (21)$$

where  $\sigma_M$  is the free surface charge density,  $\epsilon_{\text{RP}}$  is the permittivity of the adlayer, and  $\mu_{\text{chem}}$  is the chemisorption-induced surface dipole moment<sup>58,59</sup>

$$\mu_{\text{chem}} = e\rho(\theta_{\text{HCOO}_b} \varsigma_{\text{HCOO}_b} + \theta_{\text{OH}_{ad}} \varsigma_{\text{OH}_{ad}}) \delta_{\text{RP}} \quad (22)$$

with  $\varsigma_{\text{HCOO}_b}$  and  $\varsigma_{\text{OH}_{ad}}$  being the net charge numbers of  $\text{HCOO}_b$  and  $\text{OH}_{ad}$ . The dipole moment of  $\text{HCOO}_m$  has been neglected due to the negligible coverage of this adsorbate.

All the parameters used in the PNP model are summarized in the [Supporting Information](#). The model was solved using COMSOL Multiphysics.

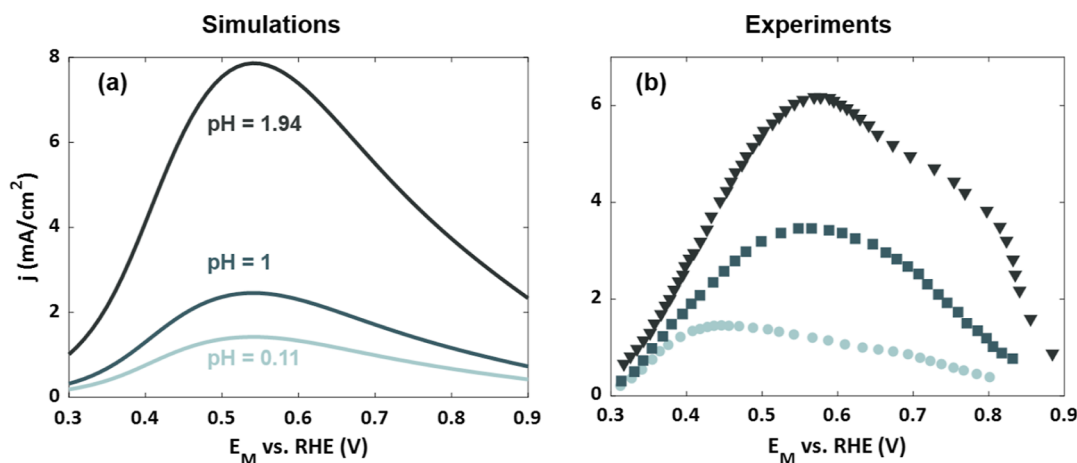


**Figure 2.** Comparison of simulated and experimental  $j$ – $E_M$  curves at pH = 0.11 (1 M HClO<sub>4</sub>), pH = 1 (0.1 M HClO<sub>4</sub>), and pH = 1.94 (0.01 M HClO<sub>4</sub> + 0.09 M NaClO<sub>4</sub>). The concentration of formic acid is 0.1 M. Experimental data are taken from ref 60.

## RESULTS

In this work, we mainly focus on the relation between the peak current density and the pH value, namely, the  $j_p$ –pH relation, which is the most discussed relation in studies of the pH effects in FAOR.<sup>24,45</sup> Our analysis begins with exclusive consideration of the microkinetics. We then add mass-transport effects and surface charging effects in sequential steps. This approach allows disentangling different factors controlling the overall pH effects.

### Intrinsic Microkinetics

We define the intrinsic microkinetics as reaction kinetics without accounting for effects of the LRE, which means that we consider  $c_i = c_{i,\text{bulk}}$ ,  $\varphi_{\text{RP}} = 0$ , and  $\sigma_M = 0$ . We start with simulating the polarization curves, namely, the  $j$ – $E_M$  curves, at different pH values using the parameters in Supporting Information Tables S1 and S2. Figure 2 compares the simulations and experiments. The model captures key features of the experimental data, namely, the  $j$ – $E_M$  curve presents a bell shape, and the activity increases with pH. However, there are quantitative differences between simulations and experiments. There could be two reasons. On the one hand, the LRE is not considered, and on the other hand, there are also noticeable discrepancies between experiments (Figure S2).

Recently, Herrero *et al.* reported that the reaction order for formate is 1.<sup>47</sup> To further validate the purported microkinetic model, we calculate the reaction order with respect to the formate concentration in solutions with pH 1.2, 2.4, and 3.9 at 0.13 V vs SHE and for concentrations of formic acid between 0.01 and 2 M. The results in Figure 3 confirm that the reaction order is nearly 1.

We then extend the model to a wide pH range. Figure 4a shows the simulated  $j$ – $E_M$  curves at pH from 0 to 12. The  $j_p$ –pH relation, obtained from Figure 4a, is shown in Figure 4b. We show that the  $j_p$ –pH relation presents a bell shape, with the peak located at pH = 6, not the  $pK_a$  of formic acid as previously thought.<sup>24,61</sup> In addition, the peak current density remains almost constant between pH 5 and 7, with a difference below 5%. We notice that in the work of Joo *et al.*<sup>24</sup> and Zhang *et al.*,<sup>61</sup>  $E_6^{\text{eq}} = 0.6$  V (SHE) is used to obtain the bell-shaped  $j_p$ –pH relation with the peak near the  $pK_a$  of formic acid. However, 0.6 V is much lower than the common equilibrium potential of OH<sub>ad</sub> adsorption at Pt(111), which is about 0.8 V,<sup>53,62</sup> resulting in an overestimation of the site-blocking effect

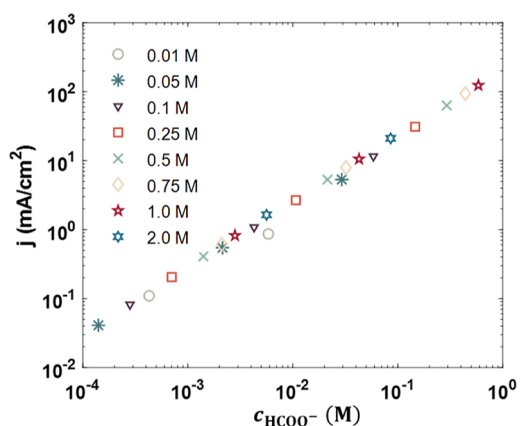


**Figure 3.** Simulated current densities at 0.13 V vs SHE as a function of the formate concentration in solutions with pH 1.2, 2.4, and 3.9. The total concentration of formic acid considered is between 0.01 and 2 M. The different symbols refer to the total formic acid concentrations.

of OH<sub>ad</sub>. The comparison of  $\theta_{\text{OH}_{\text{ad}}}$  for  $E_6^{\text{eq}} = 0.78$  V and  $E_6^{\text{eq}} = 0.6$  V is provided in Figure S3.

To understand the physical origins behind the bell-shaped  $j_p$ –pH relation, we give an analytical solution of the peak potential  $E_p$ , which is defined as the potential where the peak current density lies at a specific pH. However, since there are three adsorbates, HCOO<sub>b</sub>, HCOO<sub>m</sub> and OH<sub>ad</sub>, and HCOO<sub>b</sub> occupies two sites, the system is highly nonlinear (see eqs S1–S7), and it cannot be solved analytically. Instead of solving  $E_p$  directly, we solve  $\theta_{\text{HCOO}_b}$  and  $\theta_{\text{OH}_{\text{ad}}}$  at  $E_p$ , which is very helpful for the analysis of the  $j_p$ –pH relation. We neglect lateral interactions between adsorbates for the moment to obtain the analytical solution. The validity of this assumption will be discussed later.

Considering that HCOO<sup>−</sup> is the main reactant and the adsorption of HCOO<sub>m</sub> is the rate-determining step (see Supporting Information Note S1), the turnover frequency (TOF) can be written as

$$\text{TOF} = v_4 = k_4 c_{\text{HCOO}^-} (\theta_{\text{max}} - 2\theta_{\text{HCOO}_b} - \theta_{\text{OH}_{\text{ad}}}) \quad (23)$$

The adsorption isotherms of HCOO<sub>b</sub> and OH<sub>ad</sub> are



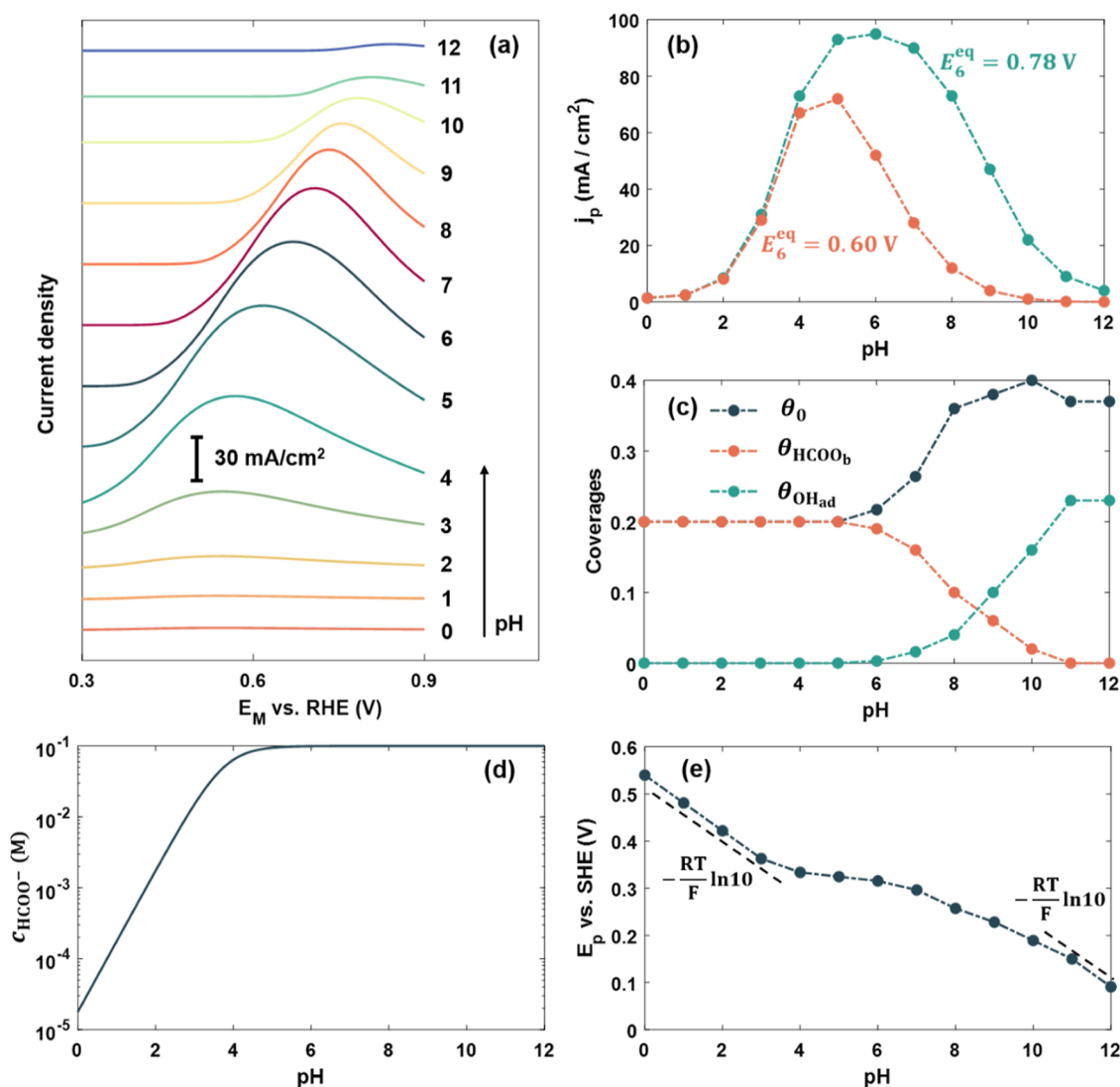


**Figure 4.** (a) Simulated  $j$ – $E_M$  curves in the pH range from 0 to 12. (b) Simulated  $j_p$ –pH relations for  $E_6^{\text{eq}} = 0.78 \text{ V}$  (used in this work) and  $E_6^{\text{eq}} = 0.60 \text{ V}$  (used in refs 24 and 61). (c) Coverages of free sites,  $\text{HCOO}_b$  and  $\text{OH}_{ad}$  at peak potentials. (d) Bulk concentration of  $\text{HCOO}^-$  at different pH values. (e) Peak potentials on the SHE scale,  $E_{p,\text{SHE}}$ .

$$\frac{(\theta_{\text{max}} - 2\theta_{\text{HCOO}_b} - \theta_{\text{OH}_{ad}})^2}{\theta_{\text{HCOO}_b}} = \frac{1}{K_2[\text{HCOO}^-]} \quad (24)$$

$$\frac{\theta_{\text{max}} - 2\theta_{\text{HCOO}_b} - \theta_{\text{OH}_{ad}}}{\theta_{\text{OH}_{ad}}} = \frac{1}{K_7[\text{OH}^-]} \quad (25)$$

with  $K_i = \frac{k_i}{k_{-i}} = \exp\left(\frac{F}{RT}(E_M - E_i^{\text{eq}})\right)$  being the equilibrium constant of step  $i$ .

At the peak potential, we have  $\frac{\partial \text{TOF}}{\partial E_M} = 0$ . Differentiating eq 23 with respect to  $E_M$ , we obtain

$$2\frac{\partial \theta_{\text{HCOO}_b}}{\partial E_M} + \frac{\partial \theta_{\text{OH}_{ad}}}{\partial E_M} = \frac{\beta_4 F}{RT}(\theta_{\text{max}} - 2\theta_{\text{HCOO}_b} - \theta_{\text{OH}_{ad}}) \quad (26)$$

Differentiating eqs 24 and 25 with respect to  $E_M$ , we then find

$$4\frac{\partial \theta_{\text{HCOO}_b}}{\partial E_M} + 2\frac{\partial \theta_{\text{OH}_{ad}}}{\partial E_M} + \frac{(\theta_{\text{max}} - 2\theta_{\text{HCOO}_b} - \theta_{\text{OH}_{ad}})}{\theta_{\text{HCOO}_b}} \frac{\partial \theta_{\text{HCOO}_b}}{\partial E_M} = \frac{F}{RT}(\theta_{\text{max}} - 2\theta_{\text{HCOO}_b} - \theta_{\text{OH}_{ad}}) \quad (27)$$

$$2\frac{\partial \theta_{\text{HCOO}_b}}{\partial E_M} + \frac{\partial \theta_{\text{OH}_{ad}}}{\partial E_M} + \frac{(\theta_{\text{max}} - 2\theta_{\text{HCOO}_b} - \theta_{\text{OH}_{ad}})}{\theta_{\text{OH}_{ad}}} \frac{\partial \theta_{\text{OH}_{ad}}}{\partial E_M} = \frac{F}{RT}(\theta_{\text{max}} - 2\theta_{\text{HCOO}_b} - \theta_{\text{OH}_{ad}}) \quad (28)$$

Solving eqs 26, 27 and 28 together, we get

$$2\frac{1 - \beta_4}{\beta_4}\theta_{\text{HCOO}_b} + \frac{1}{\beta_4}\theta_{\text{OH}_{ad}} = \theta_{\text{max}} \quad (29)$$

where  $\theta_{\text{max}} = 0.6$  and  $\beta_4 = 0.4$  (see Supporting Information Note S1) in this work. In the case where the  $\text{OH}_{ad}$  adsorption can be negligible, for example at acidic pH,<sup>63</sup> we have

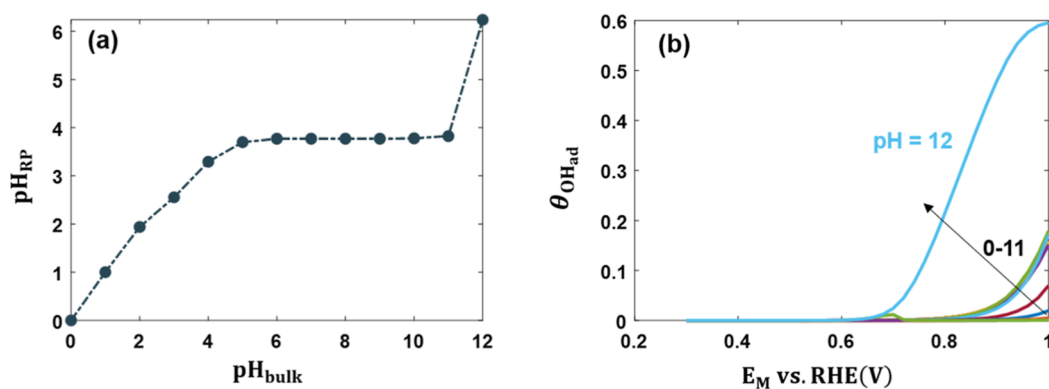


**Figure 5.** (a) Comparison of the surface pH and the bulk pH at peak potentials. (b) Adsorption isotherm of OH<sub>ad</sub> in the pH range of 0 and 12.

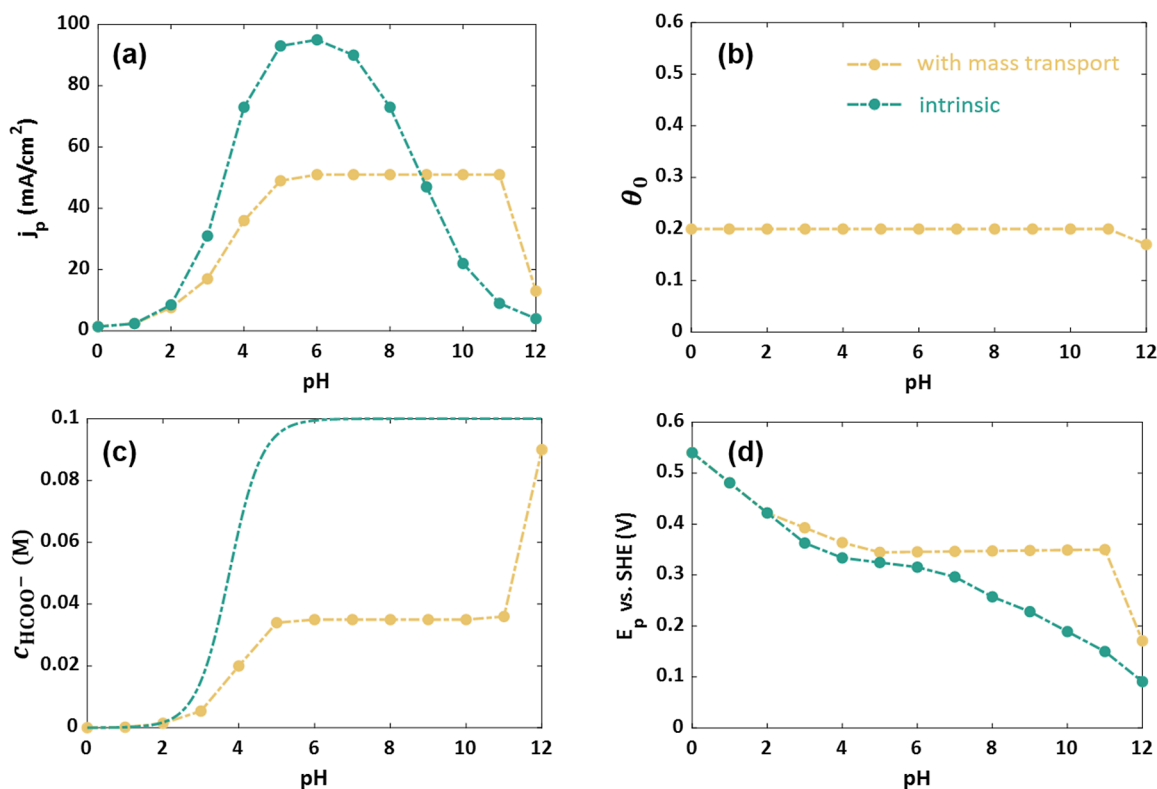


**Figure 6.** (a) Comparison of the  $j_p$ -pH relation considering only intrinsic microkinetics and the  $j_p$ -pH relation corrected by mass-transport effects. (b) Coverage of free sites at peak potentials. (c) Comparison of the bulk and the surface concentrations of HCOO<sup>-</sup>. (d) Comparison of the intrinsic microkinetics controlled peak potentials and the mass-transport-corrected peak potentials.

$$\theta_{\text{HCOO}_b} = \frac{1}{2} \frac{\beta_4}{1 - \beta_4} \theta_{\text{max}} = 0.2 \quad (30)$$

The peak potential only exists when  $\beta_4 < 0.5$  since  $\theta_{\text{HCOO}_b} < \frac{1}{2} \theta_{\text{max}}$  (HCOO<sub>b</sub> occupies two sites). The sensitivity of  $\beta_4$  in the  $j$ - $E_M$  curve at pH = 1 is shown in Figure S4.

In the case where the HCOO<sub>b</sub> adsorption can be negligible, we have

$$\theta_{\text{OH}_{ad}} = \beta_4 \theta_{\text{max}} = 0.24 \quad (31)$$

The peak potential always exists in this case. Numerical calculations considering the lateral interactions do not alter the above conclusion, as shown in Figure S5.

The simulated peak potentials lie at  $\theta_{\text{HCOO}_b} = 0.2$  when pH < 5, in which case the OH<sub>ad</sub> adsorption is negligible, as shown

in Figure 4c. This is consistent with the analytical expression of eq 30. Specifically,  $c_{\text{HCOO}^-}$  shown in Figure 4d increases approximately 10 times if pH increases by 1 when pH < 3 due to the dissociation equilibrium of formic acid. Therefore, the peak potential  $E_{p,\text{SHE}}$  must decrease by  $\frac{RT}{F} \ln 10$  to maintain  $\theta_{\text{HCOO}_b} = 0.2$  according to eq 24, as shown in Figure 4e. The peak current density will accordingly increase by  $\exp\left(-\frac{\beta_4 F}{RT} \ln 10\right) \times 10 = 10^{0.6} \approx 4$  times since  $\theta_0$  is constant. When  $5 < \text{pH} < 10$ ,  $c_{\text{HCOO}^-}$  is constant,  $E_{p,\text{SHE}}$  decreases, and  $\theta_0$  increases, resulting in a nonmonotonic  $j_p$ -pH relation. The adsorption of OH<sub>ad</sub> is dominant, and the adsorption of HCOO<sub>b</sub> is negligible when  $11 < \text{pH} < 12$ . Therefore,  $E_{p,\text{SHE}}$  decreases by  $\frac{RT}{F} \ln 10$  to keep  $\theta_{\text{OH}_{ad}} = 0.24$  according to eq 25, leading to a decrease in activity.

## Mass-Transport Effects

In this section, we add mass transport of species into the play, while the effects of surface charging are not yet considered, *i.e.*,  $\varphi_{\text{RP}} = 0$  and  $\sigma_{\text{M}} = 0$ . Since the FAOR generates protons, the solution phase in close proximity to the electrode surface should be more acidic than the solution phase in the bulk. Figure 5a shows the simulated behavior of the pH at the RP,  $\text{pH}_{\text{RP}}$ , at the peak potential as a function of the bulk pH.  $\text{pH}_{\text{RP}}$  deviates strongly from the bulk pH for  $\text{pH}_{\text{bulk}} > 4$ . In the range of  $5 < \text{pH}_{\text{bulk}} < 11$ ,  $\text{pH}_{\text{RP}}$  remains constant at  $\text{pH}_{\text{RP}} \approx 4$ , which is consistent with previous simulations.<sup>25</sup> Due to the inhibited growth of  $\text{pH}_{\text{RP}}$  with  $\text{pH}_{\text{bulk}}$ ,  $\text{OH}_{\text{ad}}$  adsorption is suppressed, as shown in Figure 5b. For comparison, the isotherm of  $\text{OH}_{\text{ad}}$  adsorption without accounting for mass-transport effects is provided in Figure S6.

Under the influence of mass-transport effects, the  $j_{\text{p}}$ –pH relation transforms from a bell shape to a trapezoidal shape, with a plateau between pH 5 and 11, as shown in Figure 6a. In this pH range,  $\text{OH}_{\text{ad}}$  adsorption is negligible, Figure 5b. Therefore, the peak potential remains at  $\theta_{\text{HCOO}_b} = 0.2$ , as shown in Figure 6b. We show  $\theta_0$  here since  $\theta_0 = \theta_{\text{max}} - 2\theta_{\text{HCOO}_b} = 0.2 = \theta_{\text{HCOO}_b}$ . The isotherm of  $\text{HCOO}_b$  adsorption given in Figure S7 is consistent with the trend in experimental data in refs 26 and 64. Since  $c_{\text{HCOO}^-}$  at the RP is constant in this pH range, as seen in Figure 6c,  $E_{\text{p,SHE}}$  must be fixed to maintain  $\theta_{\text{HCOO}_b} = 0.2$ , Figure 6d. The activity therefore remains constant according to eq 23.

In addition, mass transport exerts two competing effects: decreasing the reactant concentration  $c_{\text{HCOO}^-}$  at the RP, Figure 6c, and increasing the driving force, Figure 6d, by suppressing the  $\text{OH}_{\text{ad}}$  adsorption. When  $\text{pH} < 9$ , the effect of decreasing  $c_{\text{HCOO}^-}$  dominates, leading to a decrease in activity. When  $\text{pH} > 9$ , the effect of increasing the driving force dominates, which promotes the activity.

It has been proposed that the  $j_{\text{p}}$ –pH relation in phosphate solution is intrinsic because of the buffering capacity of the electrolyte.<sup>25</sup> We calculate the surface pH and the mass transport corrected  $j_{\text{p}}$ –pH relation in 0.2 M phosphate solution without considering the specific adsorption of phosphate anions. The results are shown in Figure S8. Compared with the case in perchlorate solution, the mass-transport effects are weakened due to the buffer reactions (Steps S3–S5). Correspondingly, the activity in phosphate solution is higher than that in perchlorate solution when  $\text{pH} < 9$ , contrary to the experimental observation that the activity in phosphate solution is much lower than that in perchlorate solution.<sup>24,45,49,65</sup> This discrepancy implies that the strong anion adsorption in phosphate solution plays a more important role than its buffering capacity. In a further step, we include the specific adsorption of phosphate anions (Step 8) in the microkinetics. The result in Figure 7 shows that the  $j_{\text{p}}$ –pH relation in phosphate solution is bell-shaped with the peak at  $\text{pH} = 6$ . This trend is consistent with experimental data on Pt(111) in ref 51. However, on polycrystalline Pt, the peak is located at  $\text{pH} = 4$ .<sup>24,45</sup> This may be due to the fact that adsorption of phosphate anions on polycrystalline Pt is different from that on Pt(111).<sup>66</sup> In addition, Figure 7 shows that the site-blocking effect of adsorbed phosphate is negligible when  $\text{pH} < 4$  and becomes significant when  $\text{pH} > 6$ , in agreement with the concentration profile of  $\text{HPO}_4^{2-}$  versus pH. Unlike  $\text{HPO}_4^{2-}$ , whose concentration is pH-dependent, added  $\text{Cl}^-$  has a pH-independent concentration. Therefore, the site-

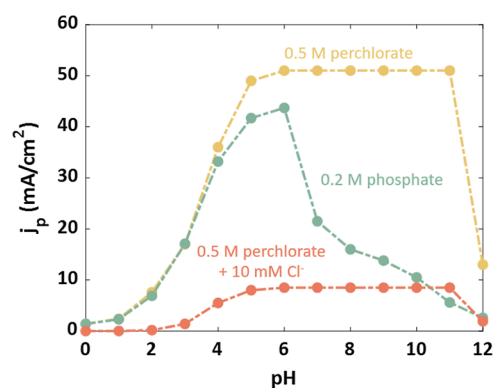


**Figure 7.** Mass-transport-corrected  $j_{\text{p}}$ –pH relations in 0.5 M perchlorate, 0.2 M phosphate, and 0.5 M perchlorate + 10 mM chloride solutions.

blocking effect of  $\text{Cl}^-$  is significant at any pH. The simulated  $j_{\text{p}}$ –pH relation in perchlorate solution containing 10 mM  $\text{Cl}^-$  captures the experimental trend in ref 45.

## Surface Charging Effects

So far, we have explained the physical origin of the experimentally observed trapezoidal-shaped  $j_{\text{p}}$ –pH relation in perchlorate solution by combining microkinetic modeling with mass-transport effects in the previous section.<sup>45</sup> However, we notice that the simulated current density in the plateau region is about three times higher than the experimental data.<sup>43,45</sup> One may assume that this is due to the underestimation of mass-transport effects. Therefore, we examine the sensitivity of the diffusion layer thickness. As shown in Figure S9, the simulated current density in the flat region is still about two times higher than the experiments even we increase  $\delta_{\text{D}}$  to 30  $\mu\text{m}$ , which corresponds to  $\omega = 350$  rpm, while the experiments are usually conducted in  $\omega > 1000$  rpm.<sup>45</sup> Analytically, we have found that  $j_{\text{p}}$  increases by about four times if pH increases by 1 when  $\text{pH} < 3$ , which means that  $j_{\text{p}} = 16$   $\text{mA}/\text{cm}^2$  at  $\text{pH} = 3$  if  $j_{\text{p}} = 1$   $\text{mA}/\text{cm}^2$  at  $\text{pH} = 1$ , while experiments give  $j_{\text{p}} \approx 3$   $\text{mA}/\text{cm}^2$  at  $\text{pH} = 1$ .<sup>60,67</sup> Combined, there should be other factors that affect the  $j_{\text{p}}$ –pH relation, and we are about to show that surface charging effects are very likely responsible for this. The surface charging effects considered in this work contain two aspects, *i.e.*, the Frumkin effects that the reactant concentration and potential at the RP are controlled not only by the mass-transport effects but also by the electrode surface charge density, and the Gibbs free energies of intermediates that depend on it.

We first consider the Frumkin corrections. The simulated  $j_{\text{p}}$ –pH relation is shown in Figure 8. Compared with the case of that includes mass-transport effects only, the inclusion of Frumkin corrections does not significantly change the trend but only slightly reduces the activity. This is because the negative surface charge has two competing impacts (as shown in Figure 1): it increases the driving force and decreases the surface concentration of  $\text{HCOO}^-$ ,  $c_{\text{HCOO}^-}$  (opposite for positive surface charge). The two competing effects more or less cancel each other off in this case. This balance is not sensitive to the key parameters of the EDL,  $\epsilon_{\text{RP}}$  and  $\delta_{\text{RP}}$ , as shown in Figure S10. Comparison of the  $j_{\text{p}}$ –pH relations corrected by only mass-transport effects and the  $j_{\text{p}}$ –pH relations corrected by Frumkin corrections in phosphate and chloride-containing solutions is shown in Figure S11.

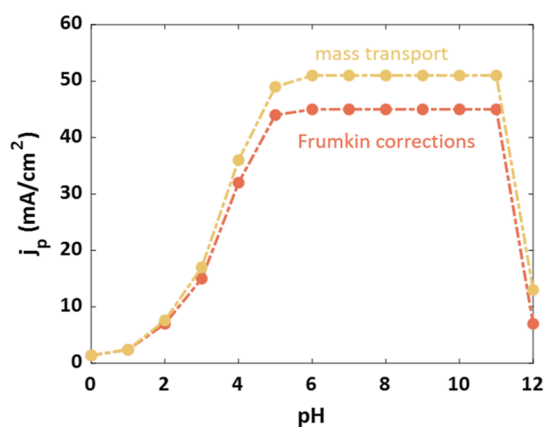


**Figure 8.** Comparison of the  $j_p$ –pH relation corrected by only mass-transport effects and the  $j_p$ –pH relation corrected by Frumkin corrections in perchlorate solution.

Recent theoretical studies have shown that the formation energies of adsorbates are dependent on the surface charge.<sup>57,68</sup> Moreover, it has been proposed that the positive surface charge is more favorable for formate adsorption.<sup>44,69</sup> To include such surface charge effects beyond Frumkin corrections, we assume that variations in the Gibbs free energies of adsorption of  $\text{HCOO}_b$  and  $\text{HCOO}_m$  are linearly correlated with the surface charge density

$$\Delta\Delta G_{\text{HCOO}_m} = \chi_1 \sigma_M h(\sigma_M) + \chi_2 \sigma_M h(-\sigma_M) \quad (32)$$

$$\Delta\Delta G_{\text{HCOO}_b} = \chi_3 \sigma_M h(\sigma_M) + \chi_4 \sigma_M h(-\sigma_M) \quad (33)$$

where  $h(\sigma_M) = 1$  for  $\sigma_M > 0$  and  $h(\sigma_M) = 0$  otherwise,  $\chi_1 = \chi_3 = \chi_4 = -3 \text{ eV}/(\text{C}/\text{m}^2)$ ,  $\chi_2 = -12 \text{ eV}/(\text{C}/\text{m}^2)$ . eqs 32 and 33 imply that a positive surface charge density supports the formate adsorption while a negative surface charge density suppresses it. The suppression effect is more pronounced for  $\text{HCOO}_m$ .

The surface charge becomes more negative with increasing pH (Figure S12) since  $\phi_{\text{pzc}}$  on the reversible hydrogen electrode (RHE) scale increases 0.059 with pH increasing by 1. Due to the negative shift of the surface charge density, the adsorption of  $\text{HCOO}_m$  is suppressed, and the activity is reduced correspondingly. As shown in Figure 9, we achieve quantitative agreement with experiments after taking into account the surface charging effect on the free energies of intermediates. In addition, the  $j_p$ –pH relation is sensitive to the activation barrier of the key reaction step,  $G_{a,4}^{\text{eq}}$ . A range of only 0.02 eV for this parameter can cover the experimental fluctuations. This implies that kinetic factors must be taken into account in model-based analyses of electrocatalytic activity.

The polarization curve is also affected by surface charging effects. The surface charging relation is nonmonotonic in the adsorption region (Figure S12) since we have considered the partially charged adsorbates (eq 22) in this model.<sup>58</sup> Therefore, the increase of negative surface charge induced by the dipole moment of the adsorbates suppresses the activity by inhibiting the adsorption of formate (eqs 32 and 33). As shown in Figure S13, the simulated  $j$ – $E_M$  curve transforms from a bell shape to a camel shape, with a valley in the adsorption region of  $\text{HCOO}_b$ . This phenomenon is observed in the experiments of FAOR on a polycrystalline Pt electrode.<sup>49</sup> However, it is not

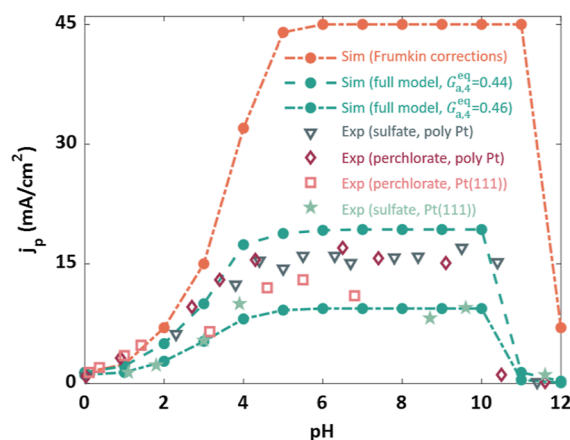


**Figure 9.** Comparison of the simulated  $j_p$ –pH relations and the experimental  $j_p$ –pH relations in perchlorate and sulfate solutions. The concentration of formic acid is 0.1 M. The sensitivity of  $G_{a,4}^{\text{eq}}$  is examined to cover the experimental fluctuations. Experimental data for polycrystalline Pt are taken from ref 45, for Pt(111) in perchlorate solution from ref 43, and for Pt(111) in sulfate solution from ref 25.

observed in experiments on a Pt(111) electrode.<sup>43</sup> The reason for this discrepancy might be the oversimplification of the surface charging effect as accounted for in the Gibbs free energies of adsorbates. Detailed atomic calculations will be needed to describe this relation more accurately.

We have furthermore examined our model by comparison with experimental data for formic acid oxidation in phosphate and chloride-containing solutions. Simulations done with the full model closely reproduce the experimental data, as can be seen in Figure 10. The quantitative agreement demonstrates that the full model reliably captures the interplay of intrinsic kinetics, mass transport, and surface charging effects in different solutions.

## DISCUSSION

In this section, we first provide a critical account of various explanations for the peculiar pH effects in the FAOR. Then, we address limitations of the model and discuss extensions needed to generalize the model.

### Critical Review of Existing Explanations

There have been several explanations for the pH effects in FAOR. Joo *et al.* observed a bell-shaped  $j_p$ –pH relation on Pt with the peak at  $\text{pK}_a$ . They explained this phenomenon as follows. When  $\text{pH} < \text{pK}_a$ , the concentration of  $\text{HCOO}^-$  increases with pH, the activity increases since  $\text{HCOO}^-$  is the main reactant. When  $\text{pH} > \text{pK}_a$ , the site-blocking effect of  $\text{OH}_{\text{ad}}$  adsorption decreases the activity.<sup>24</sup> Brimaud *et al.* also obtained a bell-shaped relation on Au. However, the  $\text{OH}_{\text{ad}}$  adsorption is negligible on Au in the potential range of interest. They then proposed that the main reactant is not  $\text{HCOO}^-$ , but the  $[\text{HCOOH} \cdots \text{HCOO}^-]$  dimer, which has the highest concentration at  $\text{pK}_a$ .<sup>49</sup>

However, recent experiments have shown that the  $j_p$ –pH relation in perchlorate/sulfate solutions presents a trapezoidal shape with a plateau between pH 5 and 10.<sup>26,45</sup> Neither of the above two mechanisms can explain this phenomenon. Perales-Rondón *et al.* noticed that the bell-shaped  $j_p$ –pH relation in ref 24 is obtained in phosphate solution. Therefore, they stressed the site-blocking effect of adsorbed phosphate anions and attributed the plateau region to the constant concentration of



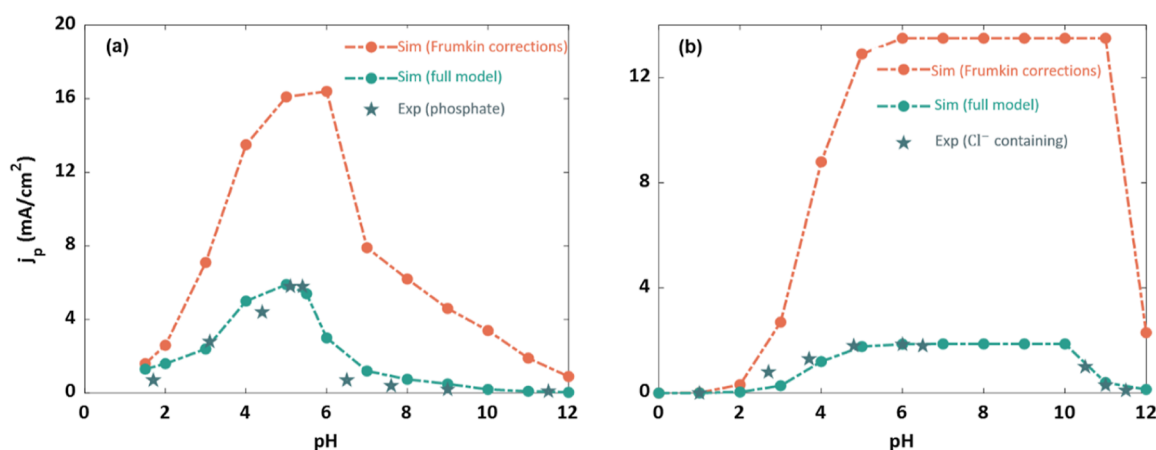


**Figure 10.** Comparison of the simulated  $j_p$ –pH relations and the experimental  $j_p$ –pH relations in (a) 0.2 M phosphate solution and (b) 0.5 M perchlorate + 10 mM chloride solution. The temperature is 20 °C in phosphate solution and 25 °C in chloride-containing solution in experiments. The concentration of formic acid is 0.05 M in phosphate solution and 0.1 M in chloride-containing solution. Experimental data for Pt(111) in phosphate solution are taken from ref 51 and those for polycrystalline Pt in chloride-containing solution from ref 45.

reactant  $\text{HCOO}^-$ .<sup>45,49</sup> In contrast, Zhang *et al.* proposed that the  $j_p$ –pH relation in phosphate solution is intrinsic due to the buffering capacity of the electrolyte, while the site-blocking effect of adsorbed phosphate anions is not important. They conjectured that the plateau region in non-buffered perchlorate solution might be caused by the local pH shift.<sup>25</sup> However, because their model did not include the effects of local pH and reactant concentration on the microkinetics, they were unable to find a consistent physical explanation of the experimental observation.

In addition, the activity, which is proportional to  $k_4 c_{\text{HCOO}^-} \theta_0$ , is not solely determined by the reactant concentration or the surface pH. There are three factors, the rate constant, the reactant concentration, and the abundance of free surface sites, that control the activity. Specifically, the rate constant,  $k_i \propto \exp\left(\frac{e(E_M - \varphi_{\text{RP}} - E_i^{\text{eq}})}{k_B T}\right)$ , wherein the driving force is defined as  $E_{\text{M,RHE}} - 0.059\text{pH}_{\text{bulk}} - \varphi_{\text{RP}}$ , does not explicitly depend on the surface pH but the bulk pH of the solution. In addition,  $\varphi_{\text{RP}}$ , which is controlled by the surface charge density, changes with pH (Figure S14). The reactant concentration is not only dictated by the surface pH since the dissociation reaction of a weak acid does not remain in equilibrium during the reaction process.<sup>70</sup> As shown in Figure S15, the water dissociation deviates from the equilibrium state when  $\text{pH} = 12$ . The coverage of free sites  $\theta_0 = \theta_{\text{max}} - 2\theta_{\text{HCOO}_b} - \theta_{\text{OH}_{\text{ad}}}$  depends not only on  $\text{OH}_{\text{ad}}$  adsorption but also on  $\text{HCOO}_b$  adsorption. By combining microkinetic modeling and LRE effects, we resolve the discrepancy on the pH effects in FAOR: (1) the intrinsic kinetic  $j_p$ –pH relation exhibits a bell shape with the peak at a pH close to 6; (2) in perchlorate solution, the surface pH remains constant around 4 between pH 5 and 10 due to the mass transport, which inhibits the adsorption of  $\text{OH}_{\text{ad}}$  and hereby leads to constant  $c_{\text{HCOO}^-}$ ,  $E_{\text{p,SHE}}$  and  $\theta_0$ , thus resulting in the plateau region; (3) in phosphate solution, the site-blocking effect of adsorbed phosphate is negligible when  $\text{pH} < 4$  and becomes significant when  $\text{pH} > 6$ , resulting in a bell-shaped  $j_p$ –pH relation with the peak at  $\text{pH} = 6$ , but this is not the intrinsic kinetic  $j_p$ –pH relation; in perchlorate solution containing  $\text{Cl}^-$ , the site-blocking effect of  $\text{Cl}^-$  is significant at any pH, resulting in a plateau region between pH 6 and 10; and (4) the increasing negative surface charge density with pH

suppresses the activity. The latter three aspects further support the crucial message that proper consideration of the LRE is important to correctly predict pH effects of electrocatalytic reactions.

From the model presented in this work, suggestions for improving the activity of the considered reaction can be derived: the electrolyte should be kept at  $\text{pH} = 6$ , the value that results in the highest intrinsic activity of the reaction; mass transport of formate should be enhanced because formate is the main reactant; buffer electrolytes with anion chemisorption, such as phosphate, should be avoided since chemisorbed anions block the active sites on the catalyst surface; and the potential of zero charge of the catalyst should be shifted to more negative value because a negative surface charge density inhibits the activity.

### Limitations and Extensions

This section aims at putting this work into a wider context and underpinning its general significance. pH effects are ubiquitous in electrocatalysis, and they play various roles, broadly categorized into intrinsic pH effects and pH-dependent LRE. Intrinsic pH effects include the shifts in potential and reactant concentration with pH. These two factors were incorporated into a kinetic model to reproduce the volcano-shaped activity–pH relation on the RHE scale.<sup>19</sup> The more subtle LRE effects have been widely neglected until recently. Zhang *et al.*<sup>25</sup> and Lamoureux *et al.*<sup>14</sup> stressed the importance of mass transport on understanding pH effects. Compared to mass-transport phenomena, surface charging phenomena are more complex. The classical approach of handling surface charging effects is via Frumkin corrections, which describe the potential and concentration distributions in the local reaction zone. With the development of advanced experimental and theoretical tools, other surface charging effects beyond Frumkin corrections have been proposed recently. Lamoureux *et al.*,<sup>14</sup> Liu *et al.*,<sup>32</sup> and Kelly *et al.*<sup>30</sup> emphasized the impact of the electric field on adsorption energies of intermediates. The impact of surface charging on interfacial solvent reorganization energies has also been highlighted.<sup>33,34,71</sup> In addition, impacts of surface charging on activation barriers and position of the RP were proposed recently.<sup>72</sup>

A change in the solution pH affects the reaction conditions and kinetics in many ways. The framework used in this work

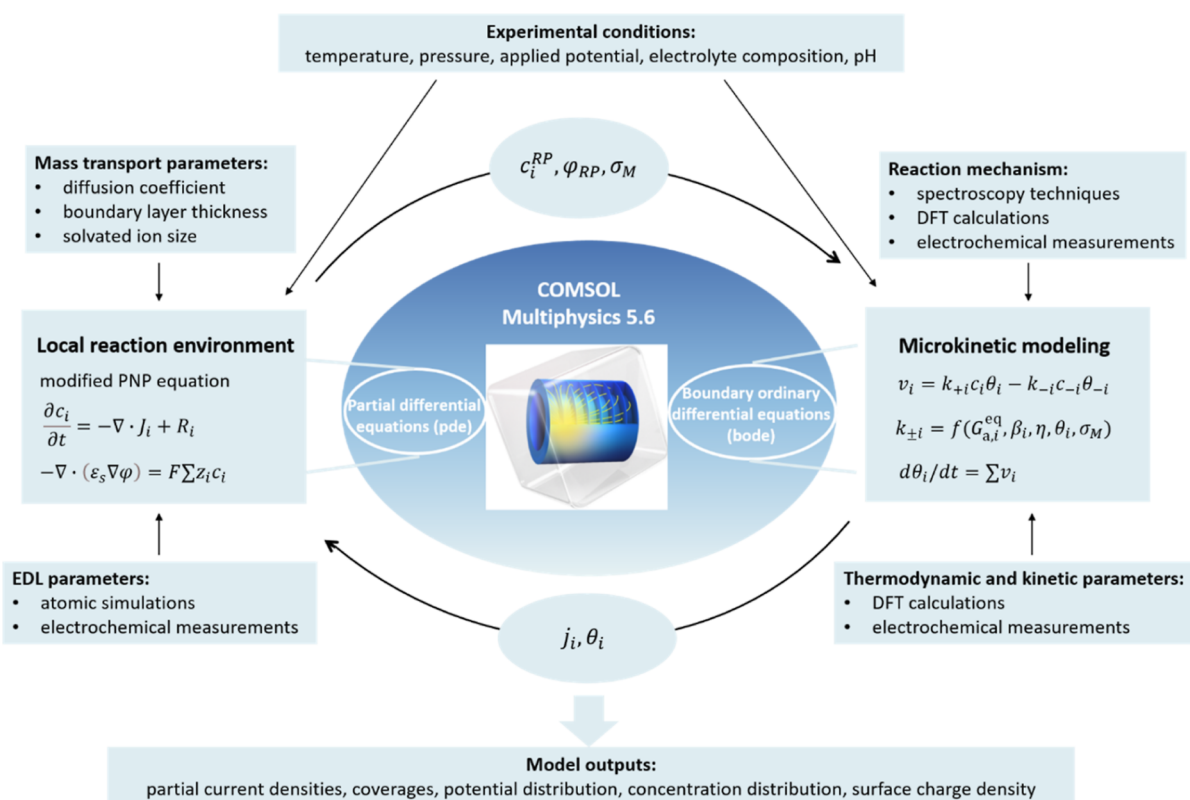


**Figure 11.** Flowchart for studying common electrochemical reactions with the framework presented in this work.

can disentangle these coupled effects. The presented framework is general, and it can be applied to decipher pH effects in other electrocatalytic reactions. To do so, the first step should be to determine the reaction mechanism of the reaction of interest and based that on build the microkinetic model with the support of DFT calculations. Analytic treatment in this step is helpful to understand the reaction metrics. Efforts along these lines have been made to understand the rate-determining term<sup>73</sup> and the Tafel slope of various electrocatalytic reactions.<sup>74</sup> The second step is to set up the model system and then build the LRE model. The mass-transport parameters, such as the diffusion layer thickness and diffusion coefficients, must be determined corresponding to the experimental conditions. Furthermore, EDL parameters, such as the configuration of adlayer and the net charge number of adsorbates, are needed, which can be obtained with the help of atomistic calculations. The flowchart for studying common electrochemical reactions using this framework is presented in Figure 11.

However, in the framework presented in this article, several assumptions and approximations have been made. First, we have used the Butler–Volmer description for the electron-transfer kinetics. However, the rate constant increases infinitely with overpotential in the Butler–Volmer approach, which is unrealistic at high overpotentials.<sup>75</sup> Advanced electron-transfer theories, for example, the Marcus–Hush theory, can be used to upgrade this framework.<sup>75</sup> In addition, Marcus–Hush theory allows for the inclusion of interfacial solvent reorganization energy. Second, we have treated the EDL as a serial connection of an adlayer and a diffuse layer. Atomic-scale understanding from first-principles calculations can be used to obtain parameters of the EDL model.<sup>76,77</sup> Third, we have assumed the surface charging effect on the adsorption energy of

intermediate simply as a linear relation. DFT-based calculations should be employed to gain explicit insights into this relation.<sup>57,68</sup> Fourth, the steady-state assumption has been used in this work. In future work, dynamic pH effects should be accounted for.

## CONCLUSIONS

In summary, we have presented a hierarchical framework to understand the pH effects in electrocatalytic reactions. Capabilities of this framework have been examined by studying the pH effects of FAOR. We have shown that the intrinsic activity–pH relation of FAOR exhibits a bell shape, but the peak is located at pH = 6, rather than at the  $pK_a$  of formic acid, deviating from previous wisdom. Mass-transport effects, which keep the surface pH close to 4 for  $5 < \text{pH} < 10$  and thus inhibit  $\text{OH}_{\text{ad}}$  adsorption, induce the activity–pH relation to transform from a bell shape to a trapezoidal shape. We have attributed the bell-shaped activity–pH relation with the peak at pH = 6 in phosphate solution to the strong adsorption of phosphate anions. The Frumkin corrections include two competing factors, *i.e.*, increasing (decreasing) the driving force and decreasing (increasing) the reactant concentration at the surface. These two factors more or less cancel each other off in this case and thus do not markedly affect the activity–pH relations. By considering the surface charging effects on the free energies of intermediates, we have obtained quantitative agreement with experimental finding. Though this work focuses on the FAOR, the framework used in this work is general and readily applicable to other electrocatalytic reactions, as has been shown.

## ■ ASSOCIATED CONTENT

### Supporting Information

The Supporting Information is available free of charge at <https://pubs.acs.org/doi/10.1021/jacsau.2c00662>.

Details of microkinetic modeling; LRE modeling; model parameters; effect of lateral interactions on the analytical solution; adsorption isotherm of  $\text{HCOO}_\text{b}$ ; buffering effects of phosphate solution; sensitivity of diffusion layer thickness; surface charging relations; and additional simulation data (PDF)

## ■ AUTHOR INFORMATION

### Corresponding Author

**Michael Eikerling** – Theory and Computation of Energy Materials (IEK-13), Institute of Energy and Climate Research, Forschungszentrum Jülich GmbH, 52425 Jülich, Germany; Chair of Theory and Computation of Energy Materials, Faculty of Georesources and Materials Engineering, RWTH Aachen University, 52062 Aachen, Germany; [orcid.org/0000-0002-0764-8948](https://orcid.org/0000-0002-0764-8948); Email: [m.eikerling@fz-juelich.de](mailto:m.eikerling@fz-juelich.de)

### Authors

**Xinwei Zhu** – Theory and Computation of Energy Materials (IEK-13), Institute of Energy and Climate Research, Forschungszentrum Jülich GmbH, 52425 Jülich, Germany; Chair of Theory and Computation of Energy Materials, Faculty of Georesources and Materials Engineering, RWTH Aachen University, 52062 Aachen, Germany; [orcid.org/0000-0002-4636-8893](https://orcid.org/0000-0002-4636-8893)

**Jun Huang** – Theory and Computation of Energy Materials (IEK-13), Institute of Energy and Climate Research, Forschungszentrum Jülich GmbH, 52425 Jülich, Germany; [orcid.org/0000-0002-1668-5361](https://orcid.org/0000-0002-1668-5361)

Complete contact information is available at: <https://pubs.acs.org/doi/10.1021/jacsau.2c00662>

### Notes

The authors declare no competing financial interest.

## ■ ACKNOWLEDGMENTS

We are grateful to Prof. Yanxia Chen for helpful discussions on this work. X.Z. and M.E. acknowledge the financial support from the Forschungszentrum Jülich GmbH and from the German-Canadian Materials Acceleration Centre (GC-MAC), which is funded by the Federal Ministry of Education and Research (BMBF) in Germany. J.H. acknowledges the funding provided by Helmholtz Young Investigators Group Leader program. The presented work was carried out within the framework of the Helmholtz program Materials and Technologies for the Energy Transition in the topic Chemical Energy Carriers and the subtopic Power-based Fuels and Chemicals.

## ■ REFERENCES

- (1) Seh, Z. W.; Kibsgaard, J.; Dickens, C. F.; Chorkendorff, I.; Nørskov, J. K.; Jaramillo, T. F. Combining Theory and Experiment in Electrocatalysis: Insights into Materials Design. *Science* **2017**, *355*, No. eaad4998.
- (2) Resasco, J.; Abild-Pedersen, F.; Hahn, C.; Bao, Z.; Koper, M. T. M.; Jaramillo, T. F. Enhancing the Connection between Computation and Experiments in Electrocatalysis. *Nat. Catal.* **2022**, *5*, 374–381.
- (3) Nitopi, S.; Bertheussen, E.; Scott, S. B.; Liu, X.; Engstfeld, A. K.; Hørch, S.; Seger, B.; Stephens, I. E. L.; Chan, K.; Hahn, C.; Nørskov, J. K.; Jaramillo, T. F.; Chorkendorff, I. Progress and Perspectives of Electrochemical  $\text{CO}_2$  Reduction on Copper in Aqueous Electrolyte. *Chem. Rev.* **2019**, *119*, 7610–7672.
- (4) Greeley, J.; Jaramillo, T. F.; Bonde, J.; Chorkendorff, I.; Nørskov, J. K. Computational High-Throughput Screening of Electrocatalytic Materials for Hydrogen Evolution. *Nat. Mater.* **2006**, *5*, 909–913.
- (5) Nørskov, J. K.; Rossmeisl, J.; Logadottir, A.; Lindqvist, L.; Kitchin, J. R.; Bligaard, T.; Jónsson, H. Origin of the Overpotential for Oxygen Reduction at a Fuel-Cell Cathode. *J. Phys. Chem. B* **2004**, *108*, 17886–17892.
- (6) Santos, E.; Quaino, P.; Schmickler, W. Theory of Electrocatalysis: Hydrogen Evolution and More. *Phys. Chem. Chem. Phys.* **2012**, *14*, 11224.
- (7) Nørskov, J. K.; Bligaard, T.; Rossmeisl, J.; Christensen, C. H. Towards the Computational Design of Solid Catalysts. *Nat. Chem.* **2009**, *1*, 37–46.
- (8) Kulkarni, A.; Siahrostami, S.; Patel, A.; Nørskov, J. K. Understanding Catalytic Activity Trends in the Oxygen Reduction Reaction. *Chem. Rev.* **2018**, *118*, 2302–2312.
- (9) Resasco, J.; Chen, L. D.; Clark, E.; Tsai, C.; Hahn, C.; Jaramillo, T. F.; Chan, K.; Bell, A. T. Promoter Effects of Alkali Metal Cations on the Electrochemical Reduction of Carbon Dioxide. *J. Am. Chem. Soc.* **2017**, *139*, 11277–11287.
- (10) Ringe, S.; Clark, E. L.; Resasco, J.; Walton, A.; Seger, B.; Bell, A. T.; Chan, K. Understanding cation effects in electrochemical  $\text{CO}_2$  reduction. *Energy Environ. Sci.* **2019**, *12*, 3001–3014.
- (11) Huang, J.; Li, M.; Eslamibidgoli, M. J.; Eikerling, M.; Groß, A. Cation Overcrowding Effect on the Oxygen Evolution Reaction. *JACS Au* **2021**, *1*, 1752–1765.
- (12) Xue, S.; Garlyyev, B.; Watzele, S.; Liang, Y.; Fichtner, J.; Pohl, M. D.; Bandarenka, A. S. Influence of Alkali Metal Cations on the Hydrogen Evolution Reaction Activity of Pt, Ir, Au, and Ag Electrodes in Alkaline Electrolytes. *ChemElectroChem* **2018**, *5*, 2326–2329.
- (13) Sheng, W.; Gasteiger, H. A.; Shao-Horn, Y. Hydrogen Oxidation and Evolution Reaction Kinetics on Platinum: Acid vs Alkaline Electrolytes. *J. Electrochem. Soc.* **2010**, *157*, B1529.
- (14) Lamoureux, P. S.; Singh, A. R.; Chan, K. PH Effects on Hydrogen Evolution and Oxidation over Pt(111): Insights from First-Principles. *ACS Catal.* **2019**, *9*, 6194–6201.
- (15) Huang, J.; Li, P.; Chen, S. Quantitative Understanding of the Sluggish Kinetics of Hydrogen Reactions in Alkaline Media Based on a Microscopic Hamiltonian Model for the Volmer Step. *J. Phys. Chem. C* **2019**, *123*, 17325–17334.
- (16) Briega-Martos, V.; Herrero, E.; Feliu, J. M. Effect of PH and Water Structure on the Oxygen Reduction Reaction on Platinum Electrodes. *Electrochim. Acta* **2017**, *241*, 497–509.
- (17) Li, M. F.; Liao, L. W.; Yuan, D. F.; Mei, D.; Chen, Y.-X. PH Effect on Oxygen Reduction Reaction at Pt(111) Electrode. *Electrochim. Acta* **2013**, *110*, 780–789.
- (18) Wang, L.; Nitopi, S. A.; Bertheussen, E.; Orazov, M.; Morales-Guio, C. G.; Liu, X.; Higgins, D. C.; Chan, K.; Nørskov, J. K.; Hahn, C.; Jaramillo, T. F. Electrochemical Carbon Monoxide Reduction on Polycrystalline Copper: Effects of Potential, Pressure, and PH on Selectivity toward Multicarbon and Oxygenated Products. *ACS Catal.* **2018**, *8*, 7445–7454.
- (19) Koper, M. T. M. Volcano Activity Relationships for Proton-Coupled Electron Transfer Reactions in Electrocatalysis. *Top. Catal.* **2015**, *58*, 1153–1158.
- (20) Rodriguez, P.; Garcia-Araez, N.; Koper, M. T. M. Self-Promotion Mechanism for CO Electrooxidation on Gold. *Phys. Chem. Chem. Phys.* **2010**, *12*, 9373–9380.
- (21) Govindarajan, N.; Xu, A.; Chan, K. How PH Affects Electrochemical Processes. *Science* **2022**, *375*, 379–380.



- (22) Kwon, Y.; Lai, S. C. S.; Rodriguez, P.; Koper, M. T. M. Electrocatalytic Oxidation of Alcohols on Gold in Alkaline Media: Base or Gold Catalysis? *J. Am. Chem. Soc.* **2011**, *133*, 6914–6917.
- (23) Lai, S. C. S.; Kleijn, S. E. F.; Öztürk, F. T. Z.; van Rees Vellinga, V. C.; Koning, J.; Rodriguez, P.; Koper, M. T. M. Effects of Electrolyte PH and Composition on the Ethanol Electro-Oxidation Reaction. *Catal. Today* **2010**, *154*, 92–104.
- (24) Joo, J.; Uchida, T.; Cuesta, A.; Koper, M. T. M.; Osawa, M. Importance of Acid-Base Equilibrium in Electrocatalytic Oxidation of Formic Acid on Platinum. *J. Am. Chem. Soc.* **2013**, *135*, 9991–9994.
- (25) Zhang, M.-K.; Wei, Z.; Chen, W.; Xu, M.-L.; Cai, J.; Chen, Y.-X. Bell Shape vs Volcano Shape PH Dependent Kinetics of the Electrochemical Oxidation of Formic Acid and Formate, Intrinsic Kinetics or Local PH Shift? *Electrochim. Acta* **2020**, *363*, 137160.
- (26) Wei, Z.; Zhang, M. K.; Zhu, B. Q.; Cai, J.; Chen, Y.-X. Mechanistic Insight into Formic Acid/Formate Oxidation at the Au(111) Electrode: Implications from the PH Effect and H/D Kinetic Isotope Effect. *J. Phys. Chem. C* **2022**, *126*, 11987–12002.
- (27) Rebollar, L.; Intikhab, S.; Snyder, J. D.; Tang, M. H. Determining the Viability of Hydroxide-Mediated Bifunctional HER/HOR Mechanisms through Single-Crystal Voltammetry and Microkinetic Modeling. *J. Electrochem. Soc.* **2018**, *165*, J3209.
- (28) Dunwell, M.; Yang, X.; Setzler, B. P.; Anibal, J.; Yan, Y.; Xu, B. Examination of Near-Electrode Concentration Gradients and Kinetic Impacts on the Electrochemical Reduction of CO<sub>2</sub> Using Surface-Enhanced Infrared Spectroscopy. *ACS Catal.* **2018**, *8*, 3999–4008.
- (29) Marcandalli, G.; Goyal, A.; Koper, M. T. M. Electrolyte Effects on the Faradaic Efficiency of CO<sub>2</sub> Reduction to CO on a Gold Electrode. *ACS Catal.* **2021**, *11*, 4936–4945.
- (30) Kelly, S. R.; Kirk, C.; Chan, K.; Nørskov, J. K. Electric Field Effects in Oxygen Reduction Kinetics: Rationalizing PH Dependence at the Pt(111), Au(111), and Au(100) Electrodes. *J. Phys. Chem. C* **2020**, *124*, 14581–14591.
- (31) Blizanac, B. B.; Lucas, C. A.; Gallagher, M. E.; Arenz, M.; Ross, P. N.; Marković, N. M. Anion Adsorption, CO Oxidation, and Oxygen Reduction Reaction on a Au(100) Surface: The PH Effect. *J. Phys. Chem. B* **2004**, *108*, 625–634.
- (32) Liu, X.; Schlexer, P.; Xiao, J.; Ji, Y.; Wang, L.; Sandberg, R. B.; Tang, M.; Brown, K. S.; Peng, H.; Ringe, S.; Hahn, C.; Jaramillo, T. F.; Nørskov, J. K.; Chan, K. PH Effects on the Electrochemical Reduction of CO(2) towards C<sub>2</sub> Products on Stepped Copper. *Nat. Commun.* **2019**, *10*, 32.
- (33) Ledezma-Yanez, I.; Wallace, W. D. Z.; Sebastián-Pascual, P.; Climent, V.; Feliu, J. M.; Koper, M. T. M. Interfacial Water Reorganization as a PH-Dependent Descriptor of the Hydrogen Evolution Rate on Platinum Electrodes. *Nat. Energy* **2017**, *2*, 1–7.
- (34) Rebollar, L.; Intikhab, S.; Oliveira, N. J.; Yan, Y.; Xu, B.; McCrum, I. T.; Snyder, J. D.; Tang, M. H. “Beyond Adsorption” Descriptors in Hydrogen Electrocatalysis. *ACS Catal.* **2020**, *10*, 14747–14762.
- (35) Chen, W.; Zhang, M.-K.; Liu, B.-Y.; Cai, J.; Chen, Y.-X. Challenges and Recent Progress in Unraveling the Intrinsic PH Effect in Electrocatalysis. *Curr. Opin. Electrochem.* **2022**, *34*, 101003.
- (36) Zhu, X.; Huang, J. Modeling Electrocatalytic Oxidation of Formic Acid at Platinum. *J. Electrochem. Soc.* **2019**, *167*, 013515.
- (37) Miki, A.; Ye, S.; Osawa, M. Surface-Enhanced IR Absorption on Platinum Nanoparticles: An Application to Real-Time Monitoring of Electrocatalytic Reactions. *Chem. Commun.* **2002**, *0*, 1500–1501.
- (38) Wang, H.-F.; Liu, Z.-P. Formic Acid Oxidation at Pt/H<sub>2</sub>O Interface from Periodic DFT Calculations Integrated with a Continuum Solvation Model. *J. Phys. Chem. C* **2009**, *113*, 17502–17508.
- (39) Sakong, S.; Groß, A. The Importance of the Electrochemical Environment in the Electro-Oxidation of Methanol on Pt(111). *ACS Catal.* **2016**, *6*, 5575–5586.
- (40) Chen, Y.-X.; Heinen, M.; Jusys, Z.; Behm, R. J. Bridge-Bonded Formate: Active Intermediate or Spectator Species in Formic Acid Oxidation on a Pt Film Electrode? *Langmuir* **2006**, *22*, 10399–10408.
- (41) Chen, Y. X.; Heinen, M.; Jusys, Z.; Behm, R. J. Kinetics and Mechanism of the Electrooxidation of Formic Acid-Spectroelectrochemical Studies in a Flow Cell. *Angew. Chem., Int. Ed.* **2006**, *45*, 981–985.
- (42) Scaranto, J.; Mavrikakis, M. HCOOH Decomposition on Pt(111): A DFT Study. *Surf. Sci.* **2016**, *648*, 201–211.
- (43) Ferre-Vilaplana, A.; Perales-Rondón, J. V.; Buso-Rogero, C.; Feliu, J. M.; Herrero, E. Formic Acid Oxidation on Platinum Electrodes: A Detailed Mechanism Supported by Experiments and Calculations on Well-Defined Surfaces. *J. Mater. Chem. A* **2017**, *5*, 21773–21784.
- (44) Busó-Rogero, C.; Ferre-Vilaplana, A.; Herrero, E.; Feliu, J. M. The Role of Formic Acid/Formate Equilibria in the Oxidation of Formic Acid on Pt (111). *Electrochem. Commun.* **2019**, *98*, 10–14.
- (45) Perales-Rondón, J. V.; Brimaud, S.; Solla-Gullón, J.; Herrero, E.; Jürgen Behm, R.; Feliu, J. M. Further Insights into the Formic Acid Oxidation Mechanism on Platinum: PH and Anion Adsorption Effects. *Electrochim. Acta* **2015**, *180*, 479–485.
- (46) Joo, J.; Uchida, T.; Cuesta, A.; Koper, M. T. M.; Osawa, M. The Effect of PH on the Electrocatalytic Oxidation of Formic Acid/Formate on Platinum: A Mechanistic Study by Surface-Enhanced Infrared Spectroscopy Coupled with Cyclic Voltammetry. *Electrochim. Acta* **2014**, *129*, 127–136.
- (47) Salamon, M. J.; Briega-Martos, V.; Cuesta, A.; Herrero, E. Insight into the Role of Adsorbed Formate in the Oxidation of Formic Acid from PH-Dependent Experiments with Pt Single-Crystal Electrodes. *J. Electroanal. Chem.* **2022**, *925*, 116886.
- (48) Grozovski, V.; Climent, V.; Herrero, E.; Feliu, J. M. Intrinsic Activity and Poisoning Rate for HCOOH Oxidation on Platinum Stepped Surfaces. *Phys. Chem. Chem. Phys.* **2010**, *12*, 8822–8831.
- (49) Brimaud, S.; Solla-Gullón, J.; Weber, I.; Feliu, J. M.; Behm, R. J. Formic Acid Electrooxidation on Noble-Metal Electrodes: Role and Mechanistic Implications of PH, Surface Structure, and Anion Adsorption. *ChemElectroChem* **2014**, *1*, 1075–1083.
- (50) Lee, H.; Habas, S. E.; Somorjai, G. A.; Yang, P. Localized Pd Overgrowth on Cubic Pt Nanocrystals for Enhanced Electrocatalytic Oxidation of Formic Acid. *J. Am. Chem. Soc.* **2008**, *130*, 5406–5407.
- (51) Abdelrahman, A.; Hermann, J. M.; Kibler, L. A. Electrocatalytic Oxidation of Formate and Formic Acid on Platinum and Gold: Study of PH Dependence with Phosphate Buffers. *Electrocatalysis* **2017**, *8*, 509–517.
- (52) Bligaard, T.; Nørskov, J. K.; Dahl, S.; Matthiesen, J.; Christensen, C. H.; Sehested, J. The Brønsted-Evans-Polanyi relation and the volcano curve in heterogeneous catalysis. *J. Catal.* **2004**, *224*, 206–217.
- (53) Hansen, H. A.; Viswanathan, V.; Nørskov, J. K. Unifying Kinetic and Thermodynamic Analysis of 2 e<sup>-</sup> and 4 e<sup>-</sup> Reduction of Oxygen on Metal Surfaces. *J. Phys. Chem. C* **2014**, *118*, 6706–6718.
- (54) Bard, A. J.; Faulkner, L. R. *Electrochemical Methods: Fundamentals and Applications*, 2nd ed.; Wiley: New York, 2001.
- (55) Zhu, X.; Huang, J.; Eikerling, M. Electrochemical CO<sub>2</sub> Reduction at Silver from a Local Perspective. *ACS Catal.* **2021**, *11*, 14521–14532.
- (56) Zhang, L.; Cai, J.; Chen, Y.; Huang, J. Modelling Electrocatalytic Reactions with a Concerted Treatment of Multistep Electron Transfer Kinetics and Local Reaction Conditions. *J. Phys.: Condens. Matter* **2021**, *33*, 504002.
- (57) Ringe, S.; Morales-Guio, C. G.; Chen, L. D.; Fields, M.; Jaramillo, T. F.; Hahn, C.; Chan, K. Double Layer Charging Driven Carbon Dioxide Adsorption Limits the Rate of Electrochemical Carbon Dioxide Reduction on Gold. *Nat. Commun.* **2020**, *11*, 33.
- (58) Huang, J. Surface Charging Behaviors of Electrocatalytic Interfaces with Partially Charged Chemisorbates. *Curr. Opin. Electrochem.* **2022**, *33*, 100938.
- (59) Huang, J.; Malek, A.; Zhang, J.; Eikerling, M. H. Non-Monotonic Surface Charging Behavior of Platinum: A Paradigm Change. *J. Phys. Chem. C* **2016**, *120*, 13587–13595.



- (60) Perales-Rondón, J. V.; Herrero, E.; Feliu, J. M. Effects of the Anion Adsorption and PH on the Formic Acid Oxidation Reaction on Pt(111) Electrodes. *Electrochim. Acta* **2014**, *140*, 511–517.
- (61) Zhang, M.-K.; Chen, W.; Wei, Z.; Xu, M.-L.; He, Z.; Cai, J.; Chen, Y.-X.; Santos, E. Mechanistic Implication of the pH Effect and H/D Kinetic Isotope Effect on HCOOH/HCOO<sup>-</sup> Oxidation at Pt Electrodes: A Study by Computer Simulation. *ACS Catal.* **2021**, *11*, 6920–6930.
- (62) Tripković, V.; Skúlason, E.; Siahrostami, S.; Nørskov, J. K.; Rossmeisl, J. The Oxygen Reduction Reaction Mechanism on Pt(111) from Density Functional Theory Calculations. *Electrochim. Acta* **2010**, *55*, 7975–7981.
- (63) Grozovski, V.; Vidal-Iglesias, F. J.; Herrero, E.; Feliu, J. M. Adsorption of Formate and Its Role as Intermediate in Formic Acid Oxidation on Platinum Electrodes. *ChemPhysChem* **2011**, *12*, 1641–1644.
- (64) Chen, X.; Granda-Marulanda, L. P.; McCrum, I. T.; Koper, M. T. M. How Palladium Inhibits CO Poisoning during Electrocatalytic Formic Acid Oxidation and Carbon Dioxide Reduction. *Nat. Commun.* **2022**, *13*, 38.
- (65) Hermann, J. M.; Abdelrahman, A.; Jacob, T.; Kibler, L. A. The Effect of PH and Anion Adsorption on Formic Acid Oxidation on Au(111) Electrodes. *Electrochim. Acta* **2021**, *385*, 138279.
- (66) Gisbert, R.; García, G.; Koper, M. T. M. Adsorption of phosphate species on poly-oriented Pt and Pt(1 1 1) electrodes over a wide range of pH. *Electrochim. Acta* **2010**, *55*, 7961–7968.
- (67) Betts, A.; Briega-Martos, V.; Cuesta, A.; Herrero, E. Adsorbed Formate Is the Last Common Intermediate in the Dual-Path Mechanism of the Electrooxidation of Formic Acid. *ACS Catal.* **2020**, *10*, 8120–8130.
- (68) Chen, L. D.; Urushihara, M.; Chan, K.; Nørskov, J. K. Electric Field Effects in Electrochemical CO<sub>2</sub> Reduction. *ACS Catal.* **2016**, *6*, 7133–7139.
- (69) Ferre-Vilaplana, A.; Perales-Rondón, J. V.; Feliu, J. M.; Herrero, E. Understanding the Effect of the Adatoms in the Formic Acid Oxidation Mechanism on Pt(111) Electrodes. *ACS Catal.* **2015**, *5*, 645–654.
- (70) Bui, J. C.; Lees, E. W.; Pant, L. M.; Zenyuk, I. V.; Bell, A. T.; Weber, A. Z. Continuum Modeling of Porous Electrodes for Electrochemical Synthesis. *Chem. Rev.* **2022**, *122*, 11022–11084.
- (71) Bangle, R. E.; Schneider, J.; Piechota, E. J.; Troian-Gautier, L.; Meyer, G. J. Electron Transfer Reorganization Energies in the Electrode-Electrolyte Double Layer. *J. Am. Chem. Soc.* **2020**, *142*, 674–679.
- (72) Huang, J.; Climent, V.; Groß, A.; Feliu, J. M. Understanding Surface Charge Effects in Electrocatalysis. Part 2: Hydrogen Peroxide Reactions at Platinum. *Chin. J. Catal.* **2022**, *43*, 2837.
- (73) Huang, J.; Zhu, X.; Eikerling, M. The Rate-Determining Term of Electrocatalytic Reactions with First-Order Kinetics. *Electrochim. Acta* **2021**, *393*, 139019.
- (74) Shinagawa, T.; Garcia-Esparza, A. T.; Takanabe, K. Insight on Tafel Slopes from a Microkinetic Analysis of Aqueous Electrocatalysis for Energy Conversion. *Sci. Rep.* **2015**, *5*, 13801.
- (75) Laborda, E.; Henstridge, M. C.; Batchelor-McAuley, C.; Compton, R. G. Asymmetric Marcus-Hush theory for voltammetry. *Chem. Soc. Rev.* **2013**, *42*, 4894–4905.
- (76) Magnussen, O. M.; Groß, A. Toward an Atomic-Scale Understanding of Electrochemical Interface Structure and Dynamics. *J. Am. Chem. Soc.* **2019**, *141*, 4777–4790.
- (77) Sakong, S.; Huang, J.; Eikerling, M.; Groß, A. The Structure of the Electric Double Layer: Atomistic versus Continuum Approaches. *Curr. Opin. Electrochem.* **2022**, *33*, 100953.

## Recommended by ACS

### Insights into the Oxygen Evolution Reaction on Graphene-Based Single-Atom Catalysts from First-Principles-Informed Microkinetic Modeling

Michael Rebarchik, Manos Mavrikakis, *et al.*

MARCH 31, 2023  
ACS CATALYSIS

READ 

### Interfacial Chemistry in the Electrocatalytic Hydrogenation of CO<sub>2</sub> over C-Supported Cu-Based Systems

Diego Gianolio, Rosa Arrigo, *et al.*

APRIL 14, 2023  
ACS CATALYSIS

READ 

### Kinetic Understanding of Catalytic Selectivity and Product Distribution of Electrochemical Carbon Dioxide Reduction Reaction

Dai-Jian Su, Zhong-Qun Tian, *et al.*

MARCH 02, 2023  
JACS AU

READ 

### Zooming into the Inner Helmholtz Plane of Pt(111)–Aqueous Solution Interfaces: Chemisorbed Water and Partially Charged Ions

Jun Huang.

JANUARY 25, 2023  
JACS AU

READ 

Get More Suggestions >